Kukkola, Jarno; Pirsto, Ville; Routimo, Mikko; Hinkkanen, Marko

Estimation of an unbalanced grid impedance using a three-phase power converter

Published in:
Proceedings of the 22nd European Conference on Power Electronics and Applications, EPE'20 ECCE Europe

DOI:
10.23919/EPE20ECCEEurope43536.2020.9215676

Published: 07/09/2020

Document Version
Peer-reviewed accepted author manuscript, also known as Final accepted manuscript or Post-print

Estimation of an Unbalanced Grid Impedance Using a Three-Phase Power Converter

Jarno Kukkola, Ville Pirsto, Mikko Routimo and Marko Hinkkanen
Aalto University
Department of Electrical Engineering and Automation
Espoo, Finland
Email: jarno.kukkola@aalto.fi

Keywords

≪Converter control≫, ≪Estimation technique≫, ≪Impedance measurement≫, ≪Three-phase system≫

Abstract

This paper proposes a real-time method for estimating an unbalanced grid impedance using a three-phase converter. In the method, a periodic single-frequency or multi-frequency excitation signal is added to the converter voltage reference. The converter measures currents and voltages at the point of common coupling. The impedance estimate is obtained from the measurements using sliding discrete Fourier transform (SDFT). The method is experimentally validated.

1. Introduction

Grid converters provide an interface between renewable energy sources and the grid. For control of these converters, the grid is often modeled as a three-phase voltage source and a balanced series impedance. The balanced impedance Z_g can be expressed with a transfer function such as $Z_\mathrm{g}(s) = sL_\mathrm{g} + R_\mathrm{g}$, where L_g is the inductance and R_g is the resistance of the grid. Several methods for estimating the balanced grid impedance using a converter have been proposed, see [1–10] and the papers cited therein. Generally, the impedance can be estimated either in the frequency domain, e.g., using the discrete Fourier transform (DFT) [1–4] or band-pass filters [5], or in the time domain applying model-based methods [6–10]. The estimation result is typically the frequency response $Z_\mathrm{g}(\mathrm{j}\omega)$ or the values of L_g and R_g. The impedance estimate can be used, e.g., to detect islanding conditions [1,5] or to optimize converter control tuning [6].

When the per-phase impedances are unequal, the grid impedance is unbalanced (asymmetric). Then, the space-vector model of the impedance becomes an asymmetric 2×2 transfer-function matrix in stationary $\alpha\beta$ coordinates [11]. Real-time estimation of the unbalanced impedance has been addressed in [12–14]. Compared to estimation of the balanced impedance, estimation of the unbalanced impedance is more complicated due to increased amount of parameters. In [12] and [13], the estimation relies on the assumption of the inductive-resistive grid. In [12], a model-based recursive least squares algorithm is used. In [13], the estimation is based on dual-frequency injection and DFTs of the currents and voltages. If the assumption of the inductive-resistive grid is violated, such as in the case of capacitive elements in the grid, these methods provide biased results. In a wavelet-based estimation method [14], this assumption is not needed. However, the method requires measurement of three line-to-neutral voltages. Therefore, contrary to the methods in [12, 13], it cannot be applied if the neutral-point is not available or only line-to-line voltages are measured.

Estimation of a 2×2 impedance matrix in synchronous (dq) coordinates has been studied in [3, 15] assuming time-invariant impedance during the estimation. If an $\alpha\beta$-asymmetric impedance is transformed to synchronous coordinates, the resulting 2×2 transfer-function matrix becomes time variant,

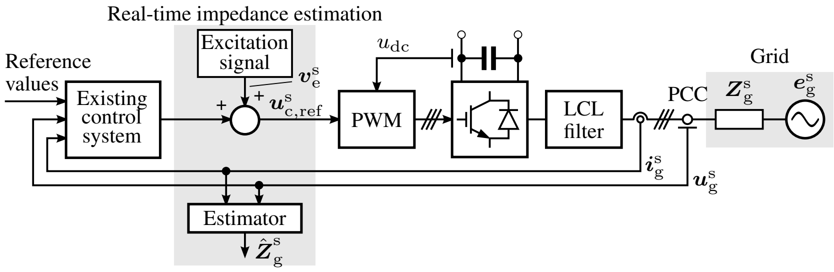

Fig. 1: Real-time grid impedance estimation as a part of the converter control system.

i.e., it depends on the angle of the coordinate system [11]. Therefore, instead of $\alpha\beta$-asymmetric systems, the methods in [3, 15] are suitable only for time-invariant dq-asymmetric grid impedances. The output impedance of a three-phase grid converter is typically asymmetric in dq coordinates [16, 17]. Hence, the grid impedance may also be time-invariant dq-asymmetric when the converters have notable effect on it.

This paper presents an SDFT-based method for real-time frequency-domain estimation of an unbalanced grid impedance in $\alpha\beta$ or dq coordinates. The method estimates the elements of the impedance matrix from two successive tests at a single frequency or multiple frequencies at the same time. To provide two linearly independent tests, an excitation signal is added to converter voltage reference in two different directions periodically, first in one direction and then in its orthogonal direction. Depending on the frequencies of interest, the excitation signal is a pulsating single-frequency or a multi-frequency space vector. Line-to-line voltages can be used in the estimator, and no a-priori assumptions on the grid type are needed. If the inductive-resistive grid is assumed, the obtained estimation result can be translated to per-phase inductances and resistances. The method is validated through simulations and experiments.

2. Model

Fig. 1 shows a control system for a three-phase grid converter. The system is augmented with a real-time grid impedance estimator. The estimator is considered as a module that can be plugged in to the existing control system. The converter is connected to the grid at the point of common coupling (PCC), and the grid is modeled as a voltage source $\boldsymbol{e}_\mathrm{g}^\mathrm{s}$ with a series impedance $\boldsymbol{Z}_\mathrm{g}^\mathrm{s}$. Three-wire system is assumed, i.e., the sum of the grid phase currents is zero $i_\mathrm{ga} + i_\mathrm{gb} + i_\mathrm{gc} = 0$, where a, b, and c mark the phases. The system is modeled with real-valued space vectors. The vector of the PCC voltage is $\boldsymbol{u}_\mathrm{g}^\mathrm{s} = [u_{\mathrm{g}\alpha}, u_{\mathrm{g}\beta}]^\mathrm{T}$, where $u_{\mathrm{g}\alpha}$ and $u_{\mathrm{g}\beta}$ are the space-vector components. The superscript s denotes stationary coordinates. The PCC voltage can be further expressed as

$$\boldsymbol{u}_\mathrm{g}^\mathrm{s}(s) = \boldsymbol{Z}_\mathrm{g}^\mathrm{s}(s)\boldsymbol{i}_\mathrm{g}^\mathrm{s}(s) + \boldsymbol{e}_\mathrm{g}^\mathrm{s}(s) \tag{1}$$

where $\boldsymbol{i}_\mathrm{g}^\mathrm{s} = [i_{\mathrm{g}\alpha}, i_{\mathrm{g}\beta}]^\mathrm{T}$ is the grid current vector and $\boldsymbol{Z}_\mathrm{g}^\mathrm{s}$ is the grid impedance

$$\boldsymbol{Z}_\mathrm{g}^\mathrm{s}(s) = \begin{bmatrix} Z_{\alpha\alpha}(s) & Z_{\alpha\beta}(s) \\ Z_{\beta\alpha}(s) & Z_{\beta\beta}(s) \end{bmatrix} \tag{2}$$

The model can be transformed to synchronous coordinates resulting in $\boldsymbol{u}_\mathrm{g}(s) = \boldsymbol{Z}_\mathrm{g}(s)\boldsymbol{i}_\mathrm{g}(s) + \boldsymbol{e}_\mathrm{g}(s)$, where $\boldsymbol{u}_\mathrm{g} = \exp\{-\mathbf{J}\vartheta_\mathrm{g}(t)\}\,\boldsymbol{u}_\mathrm{g}^\mathrm{s}$, $\boldsymbol{e}_\mathrm{g} = \exp\{-\mathbf{J}\vartheta_\mathrm{g}(t)\}\,\boldsymbol{e}_\mathrm{g}^\mathrm{s}$, $\boldsymbol{i}_\mathrm{g} = \exp\{-\mathbf{J}\vartheta_\mathrm{g}(t)\}\,\boldsymbol{i}_\mathrm{g}^\mathrm{s}$, and $\boldsymbol{Z}_\mathrm{g}$ is the grid impedance with the elements Z_dd, Z_dq, Z_qd, and Z_qq. In the transformation, ϑ_g is the angle of the coordinate system, and $\mathbf{J} = \left[\begin{smallmatrix} 0 & -1 \\ 1 & 0 \end{smallmatrix}\right]$.

The impedance $\boldsymbol{Z}_\mathrm{g}^\mathrm{s}(s)$ can represent a balanced or unbalanced system. To provide an example, let us consider a three-phase inductive-resistive grid with the per-phase inductances $L_\mathrm{ga}, L_\mathrm{gb}$, and L_gc, and resistances $R_\mathrm{ga}, R_\mathrm{gb}$, and R_gc. The per-phase impedances are $Z_\mathrm{a}(s) = sL_\mathrm{ga} + R_\mathrm{ga}$, $Z_\mathrm{b}(s) = sL_\mathrm{gb} + R_\mathrm{gb}$, and $Z_\mathrm{c}(s) = sL_\mathrm{gc} + R_\mathrm{gc}$. If the coupling between the phases is neglected, the phase voltages at the PCC can be written

$$[u_\mathrm{ga}, u_\mathrm{gb}, u_\mathrm{gc}]^\mathrm{T} = \boldsymbol{Z}_\mathrm{g}^\mathrm{abc}[i_\mathrm{ga}, i_\mathrm{gb}, i_\mathrm{gc}]^\mathrm{T} + [e_\mathrm{ga}, e_\mathrm{gb}, e_\mathrm{gc}]^\mathrm{T} \tag{3}$$

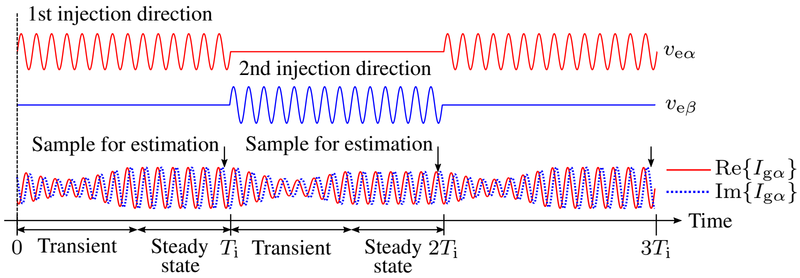

Fig. 2: Timing of the injection and estimation.

where $\boldsymbol{Z}_\mathrm{g}^\mathrm{abc}$ is a diagonal matrix $\boldsymbol{Z}_\mathrm{g}^\mathrm{abc} = \mathrm{diag}(Z_\mathrm{a}, Z_\mathrm{b}, Z_\mathrm{c})$. Transforming the phase quantities to space vectors as presented in [11], the impedance of this system in stationary coordinates becomes

$$\boldsymbol{Z}_\mathrm{g}^\mathrm{s}(s) = \boldsymbol{T}_{32}\boldsymbol{Z}_\mathrm{g}^\mathrm{abc}(s)\boldsymbol{T}_{23} = \begin{bmatrix} \frac{4Z_\mathrm{a}(s)+Z_\mathrm{b}(s)+Z_\mathrm{c}(s)}{6} & \frac{\sqrt{3}[Z_\mathrm{c}(s)-Z_\mathrm{b}(s)]}{6} \\ \frac{\sqrt{3}[Z_\mathrm{c}(s)-Z_\mathrm{b}(s)]}{6} & \frac{Z_\mathrm{b}(s)+Z_\mathrm{c}(s)}{2} \end{bmatrix}, \quad \boldsymbol{T}_{32} = \begin{bmatrix} \frac{2}{3} & -\frac{1}{3} & -\frac{1}{3} \\ 0 & \frac{1}{\sqrt{3}} & -\frac{1}{\sqrt{3}} \end{bmatrix} \tag{4}$$

where $\boldsymbol{T}_{23} = (3/2)\boldsymbol{T}_{32}^\mathrm{T}$. From (4), it can seen that if the per-phase impedances are equal $Z_\mathrm{a} = Z_\mathrm{b} = Z_\mathrm{c} = Z_\mathrm{g}$, the impedance $\boldsymbol{Z}_\mathrm{g}^\mathrm{s}$ reduces to the diagonal matrix $\boldsymbol{Z}_\mathrm{g}^\mathrm{s} = \mathrm{diag}(Z_\mathrm{g}, Z_\mathrm{g})$, but in the case of an unbalanced impedance, all elements of $\boldsymbol{Z}_\mathrm{g}^\mathrm{s}$ are generally nonzero.

3. Impedance Estimator

The frequency response of the grid impedance is estimated at a single frequency ω_e or multiple frequencies $\omega_{\mathrm{e},1}, \ldots, \omega_{\mathrm{e},n}$ at a time. For the estimation, a pulsating excitation signal $\boldsymbol{v}_\mathrm{e}^\mathrm{s}$ is added to the converter voltage reference $\boldsymbol{u}_\mathrm{c,ref}^\mathrm{s}$ as shown in Fig. 1.

3.1. Single-Frequency Estimation

For the single-frequency estimation, the excitation signal is

$$\boldsymbol{v}_\mathrm{e}^\mathrm{s}(t) = \begin{bmatrix} v_{\mathrm{e}\alpha}(t) \\ v_{\mathrm{e}\beta}(t) \end{bmatrix} = \mathrm{e}^{\mathbf{J}\vartheta_\mathrm{e}(t)} \begin{bmatrix} v_\mathrm{e}\sin(\omega_\mathrm{e}t) \\ 0 \end{bmatrix}, \qquad \mathbf{J} = \begin{bmatrix} 0 & -1 \\ 1 & 0 \end{bmatrix} \tag{5}$$

where v_e is the magnitude and ϑ_e determines the angle of the pulsating vector in stationary coordinates. In this work, the angle is alternated between $\vartheta_\mathrm{e} = 0$ and $\vartheta_\mathrm{e} = \pi/2$ to excite the system in α-axis and β-axis directions periodically

$$\begin{aligned} &\vartheta_\mathrm{e}(t) = 0, && \text{when} \quad \sin(\pi t/T_\mathrm{i}) > 0 \\ &\vartheta_\mathrm{e}(t) = \pi/2, && \text{otherwise} \end{aligned} \tag{6}$$

where T_i is the sampling interval of the impedance estimation. Two different injection directions are needed to provide two linearly independent tests for the impedance matrix identification. It is assumed that the injection-frequency component is not present in the grid voltage or current spectrum before the injection. Therefore, the frequency ω_e of the signal is a grid-frequency interharmonic. An excitation signal corresponding to (5) and (6) is shown in Fig. 2.

Fig. 3(a) shows the structure of the proposed impedance estimator in the case of single-frequency estimation. The impedance estimator utilizes the PCC voltage and current samples measured by the converter. Sampled line-to-line voltages and phase currents are turned into corresponding space-vector components $u_{\mathrm{g}\alpha}$, $u_{\mathrm{g}\beta}$, $i_{\mathrm{g}\alpha}$, and $i_{\mathrm{g}\beta}$. The complex phasors $I_{\mathrm{g}\alpha}(\omega_\mathrm{e})$ and $I_{\mathrm{g}\beta}(\omega_\mathrm{e})$ of the current components and the complex phasors $U_{\mathrm{g}\alpha}(\omega_\mathrm{e})$ and $U_{\mathrm{g}\beta}(\omega_\mathrm{e})$ of the voltage components are continuously calculated in real-time applying the modulated SDFT algorithm [18]. The internal structure of the SDFT module used in the proposed method is shown in Fig. 3(b). It is to be noted that due to the sliding window of the SDFT

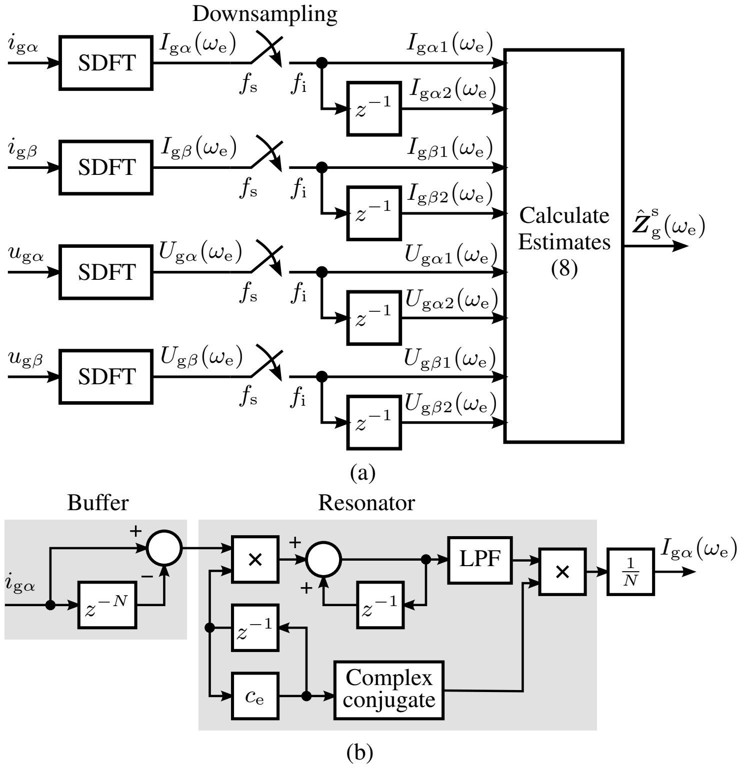

Fig. 3: (a) Proposed impedance estimator. (b) Internal structure of the SDFT module. The resonator coefficient $c_{\mathrm{e}} = \exp(-\mathrm{j}\omega_{\mathrm{e}} T_{\mathrm{s}})$ is set corresponding the angular frequency ω_{e} of the excitation.

algorithm, the calculated phasors are rotating as shown in Fig. 2.

Since the injection-frequency component of $\boldsymbol{e}_{\mathrm{g}}^{\mathrm{s}}$ is assumed to be zero, the phasors of the PCC voltage at ω_{e} can be expressed as

$$\underbrace{\begin{bmatrix} U_{\mathrm{g}\alpha 1}(\omega_{\mathrm{e}}) & U_{\mathrm{g}\alpha 2}(\omega_{\mathrm{e}}) \\ U_{\mathrm{g}\beta 1}(\omega_{\mathrm{e}}) & U_{\mathrm{g}\beta 2}(\omega_{\mathrm{e}}) \end{bmatrix}}_{\mathbf{U}_{\mathrm{m}}(\omega_{\mathrm{e}})} = \boldsymbol{Z}_{\mathrm{g}}^{\mathrm{s}}(\mathrm{j}\omega_{\mathrm{e}}) \underbrace{\begin{bmatrix} I_{\mathrm{g}\alpha 1}(\omega_{\mathrm{e}}) & I_{\mathrm{g}\alpha 2}(\omega_{\mathrm{e}}) \\ I_{\mathrm{g}\beta 1}(\omega_{\mathrm{e}}) & I_{\mathrm{g}\beta 2}(\omega_{\mathrm{e}}) \end{bmatrix}}_{\mathbf{I}_{\mathrm{m}}(\omega_{\mathrm{e}})} \tag{7}$$

where $U_{\mathrm{g}\alpha 1}, U_{\mathrm{g}\beta 1}$, $I_{\mathrm{g}\alpha 1}, I_{\mathrm{g}\beta 1}$ are obtained during the first injection direction (first test) and $U_{\mathrm{g}\alpha 2}, U_{\mathrm{g}\beta 2}$, $I_{\mathrm{g}\alpha 2}, I_{\mathrm{g}\beta 2}$ during the second injection direction (second test). Two different tests provide enough information for the impedance matrix estimation, and the estimate is directly calculated as

$$\hat{\boldsymbol{Z}}_{\mathrm{g}}^{\mathrm{s}}(\mathrm{j}\omega_{\mathrm{e}}) = \hat{\boldsymbol{R}}_{\mathrm{g}}^{\mathrm{s}}(\omega_{\mathrm{e}}) + \mathrm{j}\hat{\boldsymbol{X}}_{\mathrm{g}}^{\mathrm{s}}(\omega_{\mathrm{e}}) = \mathbf{U}_{\mathrm{m}}(\omega_{\mathrm{e}})\mathbf{I}_{\mathrm{m}}^{-1}(\omega_{\mathrm{e}}) \tag{8}$$

where $\hat{\boldsymbol{R}}_{\mathrm{g}}^{\mathrm{s}}$ and $\hat{\boldsymbol{X}}_{\mathrm{g}}^{\mathrm{s}}$ are the resistive and reactive parts of the impedance matrix.

The phasors of the voltages and currents are applicable to impedance estimation only when the system is in steady state. Since the angle ϑ_{e} of the pulsating injection (6) is periodically changed, the steady state has to be reached before the next change in ϑ_{e}. Therefore, the impedance estimation is synchronized with the excitation signal such that the rotating phasors of the currents and voltages for (8) are sampled just before the change in ϑ_{e} with the sampling frequency of $f_{\mathrm{i}} = 1/T_{\mathrm{i}}$ as illustrated in Fig. 2. The steady-state requirement sets the minimum value for the impedance estimation interval T_{i}. Moreover, the time required to reach the steady state depends on the settling time of the existing control system and phasor calculation. The settling time of the phasor calculation is related to the buffer length N of the SDFT modules, and N depends on the desired frequency resolution and sampling frequency f_{s} of the DFT. Therefore, the settling time of the phasor calculation is approximately one fundamental period of the DFT frequency resolution. The frequency resolution has to be a common divisor of the fundamental frequency of the grid and the injection frequency. To give an example, if the frequency resolution is 10

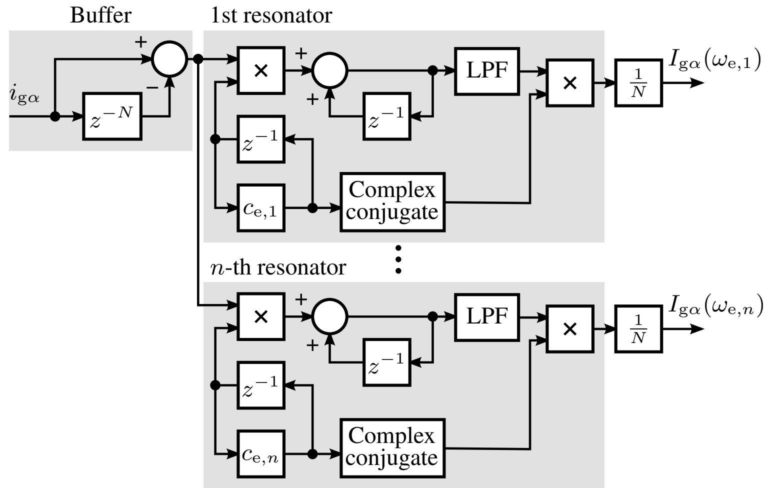

Fig. 4: SDFT module for multi-frequency phasor calculation. The resonator coefficients are set corresponding the frequencies of interest, i.e., $c_{\mathrm{e},1} = \exp(-\mathrm{j}\omega_{\mathrm{e},1}T_{\mathrm{s}}), \ldots, c_{\mathrm{e},n} = \exp(-\mathrm{j}\omega_{\mathrm{e},n}T_{\mathrm{s}})$.

Hz and the sampling frequency is $f_{\mathrm{s}} = 10$ kHz, the buffer size is $N = 1000$ and the settling time of the SDFT modules and the phasor calculation is approximately $1/(10\ \mathrm{Hz}) = 100$ ms.

When the system is in steady state, the calculated phasors can be averaged to reduce effect of measurement noise and to increase accuracy of the impedance estimation. For averaging the phasors, the SDFT structure presented in [18] is augmented with a low-pass filter (LPF). In this paper, a first-order LPF with the transfer function of $\alpha_{\mathrm{f}}/(s+\alpha_{\mathrm{f}})$ and bandwidth of α_{f} is applied due to its simplicity. It is transformed to discrete time via the mapping $s \to (z-1)/T_{\mathrm{s}}$. Alternatively, the LPF can be, e.g., a moving-average filter which is naturally averaging the phasors over its buffer length. The LPF is inserted inside the resonator, as shown in Fig. 3(b), where the signals are dc-valued in steady state.

In the SDFT module, the resonator coefficient $c_{\mathrm{e}} = \exp(-\mathrm{j}\omega_{\mathrm{e}}T_{\mathrm{s}})$ selects the frequency of the single DFT bin for the phasor calculation as explained in [19]. It is to be noted that, ω_{e} has to be integer multiple of the angular frequency resolution of the SDFT module as in the case of the conventional DFT. Finally, as Fig. 3(b) shows, only a few multiplications and additions are needed in one sampling period $T_{\mathrm{s}} = 1/f_{\mathrm{s}}$ per SDFT module meaning low computation burden that is an advantage in a real-time control system.

3.2. Multi-Frequency Estimation

The presented single-frequency estimator can be easily extended for multi-frequency impedance estimation with the following modifications: 1) n pulsating sinusoidal components are added at the frequencies of $\omega_{\mathrm{e},1}, \ldots, \omega_{\mathrm{e},n}$ to the converter voltage reference. 2) The SDFT modules are extended for multi-frequency phasor calculation adding extra resonators, one per frequency, in parallel with the first resonator as demonstrated in Fig. 4. 3) At every frequency component $\omega_{\mathrm{e},1}, \ldots, \omega_{\mathrm{e},n}$, the calculated phasors are sampled and impedance estimate (8) is calculated as explained in the previous section for a single frequency component.

The multi-frequency excitation signal is

$$\boldsymbol{v}_{\mathrm{e}}^{\mathrm{s}}(t) = \sum_{k=1}^{n} \mathrm{e}^{\mathbf{J}\vartheta_{\mathrm{e},k}(t)} \begin{bmatrix} v_{\mathrm{e},k}\sin(\omega_{\mathrm{e},k}t + \phi_{\mathrm{e},k}) \\ 0 \end{bmatrix} \tag{9}$$

where $v_{\mathrm{e},k}$ is the magnitude and $\vartheta_{\mathrm{e},k}$ is the angle of the k:th pulsating vector. In addition, every pulsating component can have different initial phase $\phi_{\mathrm{e},k}$ at $t = 0$. The angles $\vartheta_{\mathrm{e},k}$, $k = 1 \ldots n$, are alternated periodically in order to excite the system in different directions and to provide linearly independent tests for the impedance matrix identification. If the angles $\vartheta_{\mathrm{e},k}$ are set as in (6) for all components, the components will excite the system in the same direction, i.e., in α-axis and β-axis directions periodically. On the contrary, if the angle $\vartheta_{\mathrm{e},k}$ is not the same for every component, the magnitude $|\boldsymbol{v}_{\mathrm{e}}^{\mathrm{s}}(t)|$ of the signal can be reduced [20]. For example, in the case of dual-frequency excitation, selecting the angles to provide orthogonal components would minimize the magnitude. The initial phases $\phi_{\mathrm{e},k}$, $k = 1 \ldots n$, provide an additional degree of freedom to shape $\boldsymbol{v}_{\mathrm{e}}^{\mathrm{s}}(t)$. For multi-tone signals, several approaches to have been presented to select these initial phases to minimize the signal magnitude or the crest factor, e.g., [20, 21].

3.3. Estimation in Synchronous Coordinates

In Sections 3.1 and 3.2, the proposed estimator is introduced in stationary coordinates for $\alpha\beta$-asymmetric systems. In order to estimate dq-asymmetric impedances, the estimator can be transformed to synchronous (dq) coordinates. Only two modifications are needed. Firstly, the excitation signal $\boldsymbol{v}_{\mathrm{e}}$ is generated in synchronous coordinates similarly to (5) or (9) and transformed to stationary coordinates as $\boldsymbol{v}_{\mathrm{e}}^{\mathrm{s}} = \exp\left\{\mathbf{J}\vartheta_{\mathrm{g}}(t)\right\}\boldsymbol{v}_{\mathrm{e}}$, where ϑ_{g} is the angle of the synchronous coordinate system. Secondly, the PCC voltage and current vectors are transformed to synchronous coordinates before the SDFT-based phasor calculation and impedance estimation as $\boldsymbol{u}_{\mathrm{g}} = \exp\left\{-\mathbf{J}\vartheta_{\mathrm{g}}(t)\right\}\boldsymbol{u}_{\mathrm{g}}^{\mathrm{s}}$, and $\boldsymbol{i}_{\mathrm{g}} = \exp\left\{-\mathbf{J}\vartheta_{\mathrm{g}}(t)\right\}\boldsymbol{i}_{\mathrm{g}}^{\mathrm{s}}$, respectively. The angle ϑ_{g} for the transformations can be obtained, e.g., from a phase-locked loop (PLL) tracking the PCC voltage. The PLL has to include a band-stop filter at the injection frequency to provide injection-frequency free angle. If ϑ_{g} oscillates at the injection frequency, the estimated impedance can be significantly biased. With these modifications, the proposed estimator operates in synchronous coordinates and produces an impedance estimate in these coordinates instead of stationary coordinates. The estimation of a dq-asymmetric impedance may be of interest if other converters connected to the same grid have a notable impact on the impedance seen from the PCC.

3.4. Comparison

Properties of the proposed estimator are compared with those of the state-of-the-art converter-based estimators capable for unbalanced grid-impedance estimation. Whereas the methods in [13, 14] estimate the impedance in the natural (abc) reference frame, the method in [12] in the $\alpha\beta$ reference frame, and the methods in [3, 15] in the dq reference frame, the proposed estimator can be configured to estimate either an $\alpha\beta$- or dq-asymmetric impedance. Access to the neutral-point potential and phase-to-neutral voltage measurements are required in [14]. On the contrary, when the space vectors are applied in the estimation, line-to-line voltage measurements can be used and neutral point potential is not needed.

The estimation methods in [12, 13] assume inductive-resistive grid model whereas the impedance model is not fixed in [3, 14] and in the proposed method. In [15], a parametric differential-equation model is iteratively fitted to measured data. Although a parametric grid model is obtained as an estimation result in [15], the model order and structure has to be determined which complicates the estimation.

The DFT is used in the frequency-domain impedance estimation in [3, 13] which requires collecting the measurement data in a buffer before the impedance estimate can be calculated. If the number of data points is large, the calculation has to be run as a background process of the converter delaying the estimation. The method in [15] also requires buffers and background processing the measured data due to its iterative nature. On the contrary, the impedance estimate is updated recursively on a sample-by-sample basis in [12]. The advantage of the recursive calculation is that the computational load is spread over the excitation period. In the proposed method, data buffers are needed for the SDFT but the phasors are recursively calculated on a sample-by-sample basis. This reduces the computational burden compared to the conventional DFT in the case of a few frequency components in the estimation.

As presented in Sections 3.1 and 3.2, the proposed estimator can be configured for selective single- or multi-frequency estimation in a flexible manner thanks to its modular structure. In [13] two frequency components are required in the excitation signal to obtain the estimated inductance and resistance values. In [3, 12, 15] the excitation signal has wide frequency band since it is either required in the selected parametric estimation method [12, 15] or a wide-band frequency response is of interest [3]. Even though in the proposed method, the number of frequency components can be increased in the excitation signal and SDFT modules, the approach [3] with the pseudo-random binary signal excitation and the conventional DFT becomes more attractive if tens or hundreds of frequency components are of interest.

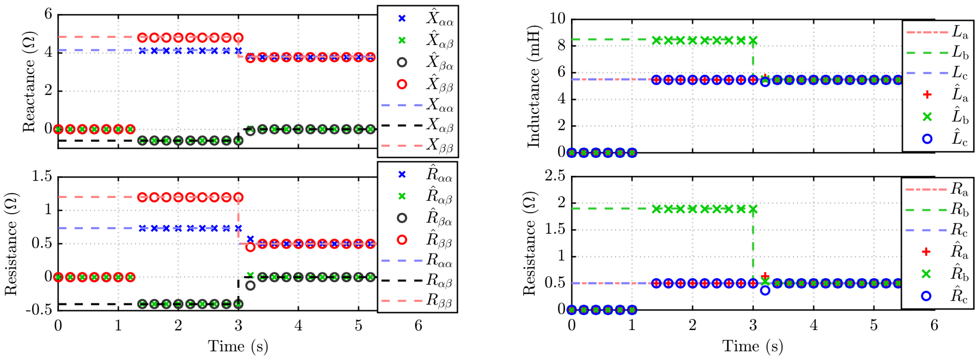

(a) (b)

Fig. 5: Simulation results: (a) estimated elements of the grid impedance matrix $\hat{\boldsymbol{Z}}_{\mathrm{g}}^{\mathrm{s}}(\omega_{\mathrm{e}}) = \hat{\boldsymbol{R}}_{\mathrm{g}}^{\mathrm{s}}(\omega_{\mathrm{e}}) + \mathrm{j}\hat{\boldsymbol{X}}_{\mathrm{g}}^{\mathrm{s}}(\omega_{\mathrm{e}})$; (b) estimated per-phase inductances and resistances. The dashed lines mark the actual values.

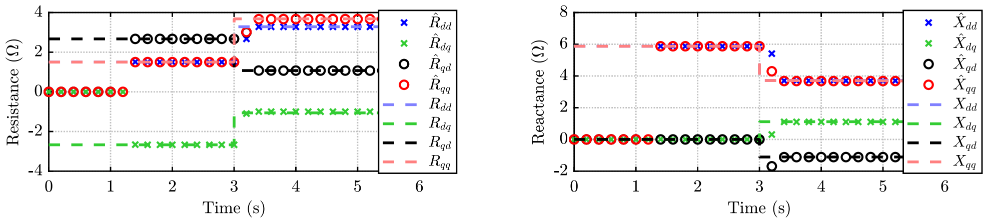

Fig. 6: Simulation results: estimated elements of the grid impedance matrix $\hat{\boldsymbol{Z}}_{\mathrm{g}}(\omega_{\mathrm{e}}) = \hat{\boldsymbol{R}}_{\mathrm{g}}(\omega_{\mathrm{e}}) + \mathrm{j}\hat{\boldsymbol{X}}_{\mathrm{g}}(\omega_{\mathrm{e}})$. The actual values are marked with dashed lines.

4. Results

4.1. Simulations

The proposed estimator is first verified with simulations considering a 400-V 12.5-kVA grid converter system. The existing control system [22] comprises a current-control loop and a PLL. The switching frequency of the converter is 5 kHz. The sampling frequency of the control system and the SDFT is $f_{\mathrm{s}} = 10$ kHz. The buffer size for the SDFT is $N = 1000$ samples per measured current or voltage component. The impedance estimation interval is set to $T_{\mathrm{i}} = 200$ ms to ensure that steady state is reached for the phasor calculation. A single-frequency excitation signal, given in (5) and (6), is used. Its frequency is an inter-harmonic of $\omega_{\mathrm{e}} = 2\pi \cdot 110$ rad/s, and its magnitude is $v_{\mathrm{e}} = 0.02$ p.u. During the verification test, the converter injects the power of $p_{\mathrm{g}} = 0.5$ p.u. to the 50-Hz grid.

Fig. 5(a) shows the estimated elements of the grid impedance matrix when the proposed method is started at $t = 1$ s to estimate an unbalanced inductive-resistive grid impedance. Per-phase inductances are $L_{\mathrm{ga}} = L_{\mathrm{gc}} = 5.5$ mH and $L_{\mathrm{gb}} = 8.5$ mH and resistances are $R_{\mathrm{ga}} = R_{\mathrm{gc}} = 0.5\ \Omega$ and $R_{\mathrm{gb}} = 1.9\ \Omega$. At $t = 3$ s the b-phase inductance L_{gb} is reduced from 8.5 mH to 5.5 mH and resistance R_{gb} is reduced from 1.9 Ω to 0.5 Ω, i.e., the impedance becomes balanced. If the inductive-resistive grid is assumed in the estimator, the estimated impedance matrix elements can be translated to per-phase inductance and resistance estimates based on (4) as $Z_{\mathrm{a}} = (3Z_{\alpha\alpha} - Z_{\beta\beta})/2$, $Z_{\mathrm{b}} = Z_{\beta\beta} - \sqrt{3}/2 \cdot (Z_{\alpha\beta} + Z_{\beta\alpha})$, and $Z_{\mathrm{c}} = Z_{\beta\beta} + \sqrt{3}/2 \cdot (Z_{\alpha\beta} + Z_{\beta\alpha})$. The per-phase estimates are demonstrated in Fig. 5(b). As the figure shows, the method correctly estimates the unbalanced and balanced grid impedance.

The capability to estimate a dq-asymmetric impedance is also verified with simulations. The estimator is configured as in the first simulation test and transformed to synchronous coordinates as described in Section 3.3. Fig. 6 shows the estimated elements of the impedance matrix when the estimator is started at $t = 1$ s to estimate a balanced grid impedance $R_{\mathrm{g}} = 1.5\ \Omega$ and $L_{\mathrm{g}} = 8.5$ mH. At $t = 3$ s, another 12.5-kVA three-phase converter with an LCL filter ($L_1 = 3.3$ mH, $C = 8.8\ \mu$F, $L_2 = 3.0$ mH) is connected to the PCC and it starts to inject active power of $p_{\mathrm{g}} = 0.5$ p.u. to the grid. Its switching frequency is 4 kHz, and its control system comprises proportional-integral (PI) grid current controller in dq coordinates

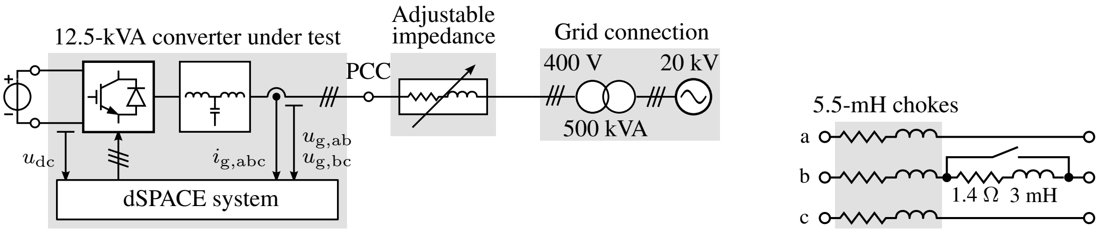

(a) (b)

Fig. 7: (a) Experimental test setup. The converter control software and the impedance estimator are running on the dSPACE DS1006 processor board where the sampling of the measured signals is synchronized with the pulse-width modulation (PWM). (b) Adjusted impedance under test.

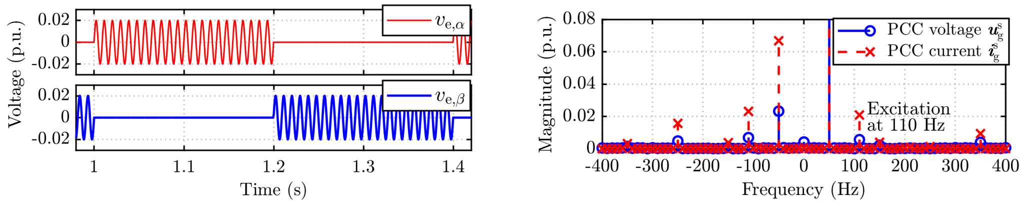

(a) (b)

Fig. 8: Measurement results: (a) excitation voltage; (b) spectra of the PCC voltage and current during the estimation.

with the cross-coupling compensation and a synchronous-reference-frame PLL (SFR-PLL). The gains of the PI controller correspond the design presented in [23] with the phase margin of $\pi/4$. The gains of the SRF-PLL are $k_{\mathrm{p,pll}} = 0.272$ $(1/\mathrm{Vs})$ and $k_{\mathrm{i,pll}} = 12.1$ $(1/\mathrm{Vs}^2)$.

As Fig. 6 shows, the other converter at the PCC significantly changes the overall grid impedance seen by the estimating converter (dashed-lines show the theoretical overall impedance). Nevertheless, the proposed estimator accurately estimates the impedance in dq coordinates with and without the other converter in the system. Furthermore, it was observed that the switching frequency components originating from the other converter can cause significant bias in the estimates. To alleviate this bias, a simple 3-kHz first-order filter was employed as an anti-aliasing filter for the PCC voltage and current measurements.

4.2. Experiments

The verification test was experimentally repeated. A diagram of the setup used in the experiments is shown in Fig. 7(a). The unbalanced impedance is emulated with 5.5-mH chokes in all three phases and an extra 3-mH choke and resistance of 1.4 Ω in the b phase as demonstrated in Fig. 7(b). The chokes are connected between the PCC and the 50-Hz electric power system. Fig. 8(a) shows the excitation signal during the experiment, and Fig. 8(b) shows the PCC current and voltage spectra when the excitation signal is enabled. The spectra are calculated over five grid-voltage periods (0.1 s) during one injection direction when the grid impedance is unbalanced. It can be seen that the magnitudes of the injection-frequency components are at the same level as typical grid current harmonics. The -50 Hz negative sequence component originates from the unbalanced impedance.

Fig. 9(a) shows the estimated elements of the grid impedance matrix and Fig. 9(b) the estimated per-phase inductances and resistances. The estimated per-phase impedances are obtained from the elements of the impedance matrix as in Section 4.1. The proposed method is started at $t = 1$ s, and the extra 3-mH choke and resistance in the b-phase is bypassed around $t = 3.5$ s [cf. Fig 7(b)] to change the impedance from unbalanced to balanced. As the results demonstrate, the proposed method can identify the balanced and unbalanced grid impedance and detect changes well in real time. Compared to the simulation results, the estimated resistive components are influenced by the noise in the measured signals causing some variance. The effect of noise can be reduced with averaging the calculated phasors as explained in Section 3.1. Here, the LPF bandwidth for this purpose was set to $\alpha_{\mathrm{f}} = 2\pi \cdot 10$ Hz.

Finally, the same test was repeated using a multi-frequency excitation signal (9) to demonstrate the

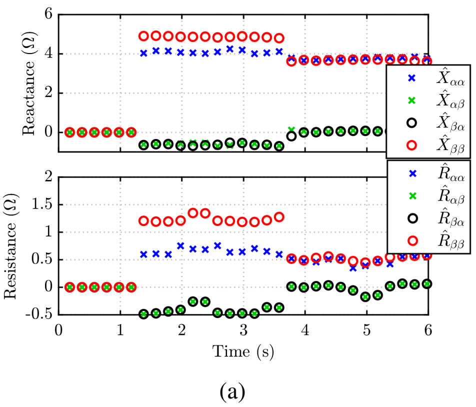

Fig. 9: Measurement results with single-frequency excitation: (a) estimated elements of the grid impedance matrix $\hat{\boldsymbol{Z}}^{\mathrm{s}}_{\mathrm{g}}(\omega_{\mathrm{e}}) = \hat{\boldsymbol{R}}^{\mathrm{s}}_{\mathrm{g}}(\omega_{\mathrm{e}}) + \mathrm{j}\hat{\boldsymbol{X}}^{\mathrm{s}}_{\mathrm{g}}(\omega_{\mathrm{e}})$; (b) estimated per-phase inductances and resistances.

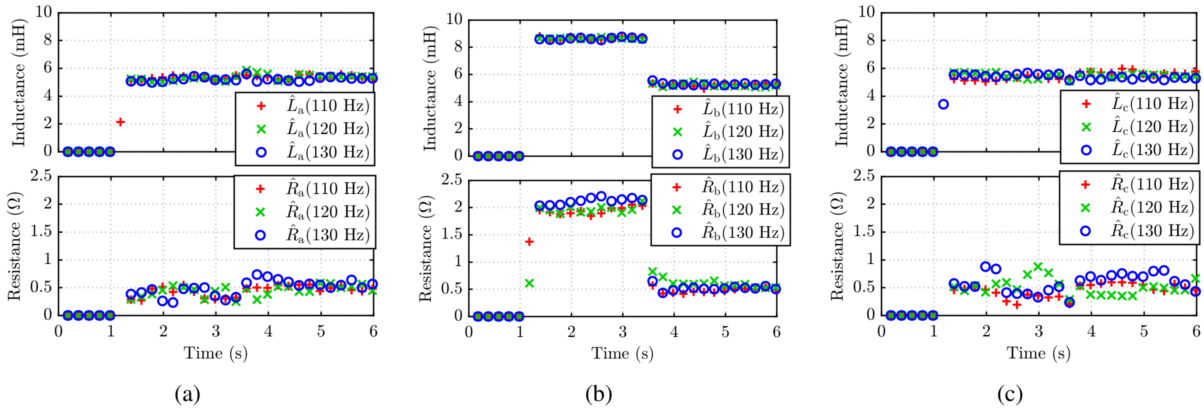

Fig. 10: Measurement results with multi-frequency excitation: (a) estimated a-phase inductances and resistances; (b) estimated b-phase inductances and resistances; (c) estimated c-phase inductances and resistances.

multi-frequency estimation. The injection frequencies are $\omega_{\mathrm{e},1} = 2\pi \cdot 110$ Hz, $\omega_{\mathrm{e},2} = 2\pi \cdot 120$ Hz, and $\omega_{\mathrm{e},3} = 2\pi \cdot 130$ Hz, and the amplitudes of the signals are $v_{\mathrm{e},1} = v_{\mathrm{e},2} = v_{\mathrm{e},3} = 0.02$ p.u. For simplicity, the injection angles $\vartheta_{\mathrm{e},k}$ are selected according to (6) and the phase shifts are $\phi_{\mathrm{e},k} = 0$ for all $k = 1 \ldots 3$. Fig. 10 shows the estimated per-phase inductances and resistances at all injection frequencies. Again, the impedance change is well detected and the estimation results at these frequencies agree with each other. A drawback of the multi-frequency estimation is increased distortion of grid currents due to multiple injection components. However, simultaneous estimation of multiple frequency components can provide more information of the grid impedance within same estimation interval. In addition, calculating the average of the estimated resistances obtained at different frequencies, e.g., $[R_{\mathrm{a}}(110\ \mathrm{Hz}) + R_{\mathrm{a}}(120\ \mathrm{Hz}) + R_{\mathrm{a}}(130\ \mathrm{Hz})]/3$, helps to reduce variance of the estimated resistances.

5. Conclusions

This paper presented a real-time grid impedance estimation method for three-phase power converters. While a periodic excitation signal is added to the converter voltage reference, the proposed method can continuously estimate either unbalanced or balanced impedance at the injection frequency. Due to lightweight computation of the SDFT algorithm used in the estimation, the proposed method can be easily implemented in a converter control system. The estimated impedance can be internally applied in the control system, e.g., to improve control performance. In remote monitoring of converters, the estimated impedance may provide added value when analyzing a converter or power system status or possible grid–converter interactions. In addition to grid converter systems, the presented estimation technique can be applied in other converter systems with similar interfaces, such as in motor drives.

References

[1] L. Asiminoaei, R. Teodorescu, F. Blaabjerg, and U. Borup, “Implementation and test of an online embedded grid impedance estimation technique for PV inverters,” *IEEE Trans. Ind. Electron.*, vol. 52, no. 4, pp. 1136–1144, Aug. 2005.

[2] M. Céspedes and J. Sun, “Online grid impedance identification for adaptive control of grid-connected inverters,” in *Proc. IEEE ECCE 2012*, Raleigh, NC, Sep. 2012, pp. 914–921.

[3] T. Roinila, T. Messo, and E. Santi, “MIMO-identification techniques for rapid impedance-based stability assessment of three-phase systems in DQ domain,” *IEEE Trans. Power Electron.*, vol. 33, no. 5, pp. 4015–4022, May 2018.

[4] A. Riccobono, M. Mirz, and A. Monti, “Noninvasive online parametric identification of three-phase AC power impedances to assess the stability of grid-tied power electronic inverters in LV networks,” *IEEE Trans. Emerg. Sel. Topics Power Electron.*, vol. 6, no. 2, pp. 629–647, Jun. 2018.

[5] D. Reigosa, F. Briz, C. B. Charro, P. García, and J. M. Guerrero, “Active islanding detection using high-frequency signal injection,” *IEEE Trans. Ind. Appl.*, vol. 48, no. 5, pp. 1588–1597, Sep. 2012.

[6] A. Vidal, A. G. Yepes, F. D. Freijedo, Ó. López, J. Malvar, F. Baneira, and J. Doval-Gandoy, “A method for identification of the equivalent inductance and resistance in the plant model of current-controlled grid-tied converters,” *IEEE Trans. Power Electron.*, vol. 30, no. 12, pp. 7245–7261, Dec. 2015.

[7] S. Cobreces, E. J. Bueno, D. Pizarro, F. J. Rodriguez, and F. Huerta, “Grid impedance monitoring system for distributed power generation electronic interfaces,” *IEEE Trans. Instrum. Meas.*, vol. 58, no. 9, pp. 3112–3121, Sep. 2009.

[8] A. K. Broen, M. Amin, E. Skjong, and M. Molinas, “Instantaneous frequency tracking of harmonic distortions for grid impedance identification based on Kalman filtering,” in *Proc. IEEE COMPEL*, Trondheim, Norway, Jun. 2016.

[9] N. Hoffmann and F. W. Fuchs, “Minimal invasive equivalent grid impedance estimation in inductive-resistive power networks using extended Kalman filter,” *IEEE Trans. Power Electron.*, vol. 29, no. 2, pp. 631–641, Feb. 2014.

[10] M. Ciobotaru, V. Agelidis, and R. Teodorescu, “Line impedance estimation using model based identification technique,” in *Proc. EPE*, Birmingham, UK, Aug. 2011.

[11] L. Harnefors, “Modeling of three-phase dynamic systems using complex transfer functions and transfer matrices,” *IEEE Trans. Ind. Electron.*, vol. 54, no. 4, pp. 2239–2248, Aug. 2007.

[12] P. García, M. Sumner, Á. Navarro-Rodríguez, J. M. Guerrero, and J. García, “Observer-based pulsed signal injection for grid impedance estimation in three-phase systems,” *IEEE Trans. Ind. Electron.*, vol. 65, no. 10, pp. 7888–7899, Oct. 2018.

[13] W. Cai, B. Liu, S. Duan, and C. Zou, “An islanding detection method based on dual-frequency harmonic current injection under grid impedance unbalanced condition,” *IEEE Trans. Ind. Informat.*, vol. 9, no. 2, pp. 1178–1187, May 2013.

[14] D. K. Alves, R. Ribeiro, F. B. Costa, T. O. A. Rocha, and J. M. Guerrero, “Wavelet-based monitor for grid impedance estimation of three-phase networks,” *IEEE Trans. Ind. Electron.*, 2020, Early access.

[15] M. A. Azzouz and E. F. El-Saadany, “Multivariable grid admittance identification for impedance stabilization of active distribution networks,” *IEEE Trans. Smart Grid*, vol. 8, no. 3, pp. 1116–1128, May 2017.

[16] B. Wen, D. Boroyevich, R. Burgos, P. Mattavelli, and Z. Shen, “Analysis of D-Q small-signal impedance of grid-tied inverters,” *IEEE Trans. Power Electron.*, vol. 31, no. 1, pp. 675–687, Jan. 2016.

[17] X. Wang, L. Harnefors, and F. Blaabjerg, “Unified impedance model of grid-connected voltage-source converters,” *IEEE Trans. Power Electron.*, vol. 33, no. 2, pp. 1775–1787, Feb. 2018.

[18] K. Duda, “Accurate, guaranteed stable, sliding discrete Fourier transform [DSP tips & tricks],” *IEEE Signal Process. Mag.*, vol. 27, no. 6, pp. 124–127, Nov. 2010.

[19] J. Kukkola, M. Routimo, and M. Hinkkanen, “Real-time grid impedance estimation using a converter,” in *Proc. IEEE ECCE 2019*, Baltimore, MD, Sep. 2019, pp. 6005–6012.

[20] M. Friese, “Multitone signals with low crest factor,” *IEEE Trans. Commun.*, vol. 45, no. 10, pp. 1338–1344, Oct. 1997.

[21] M. Schroeder, “Synthesis of low-peak-factor signals and binary sequences with low autocorrelation,” *IEEE Trans. Inf. Theory*, vol. 16, no. 1, pp. 85–89, Jan. 1970.

[22] F. M. M. Rahman, U. Riaz, J. Kukkola, M. Routimo, and M. Hinkkanen, “Observer-based current control for converters with an LCL filter: Robust design for weak grids,” in *Proc. IEEE SLED*, Helsinki, Finland, Sep. 2018, pp. 36–41.

[23] S. G. Parker, B. P. McGrath, and D. G. Holmes, “Regions of active damping control for LCL filters,” *IEEE Trans. Ind. Appl.*, vol. 50, no. 1, pp. 424–432, Jan./Feb. 2014.